

# Direct Exoplanet Detection Using L1 Norm Low-Rank Approximation<sup>\*</sup>

Hazan Daglayan<sup>1</sup>[0009–0006–4843–6913], Simon Vary<sup>1</sup>[0000–0002–9929–4357],  
Valentin Leplat<sup>2</sup>[0000–0002–3313–1547], Nicolas Gillis<sup>3</sup>[0000–0001–6423–6897], and  
P.-A. Absil<sup>1</sup>[0000–0003–2946–4178]

<sup>1</sup> ICTEAM Institute, UCLouvain, Louvain-la-Neuve, Belgium  
{hazan.daglayan,simon.vary,pa.absil}@uclouvain.be

<sup>2</sup> Center of Artificial Intelligence Technology, Skoltech, Moscow, Russia  
V.Leplat@skoltech.ru

<sup>3</sup> Dept. of Mathematics and Operational Research, University of Mons, Mons,  
Belgium  
nicolas.gillis@umons.ac.be

**Abstract.** We propose to use low-rank matrix approximation using the component-wise L1-norm for direct imaging of exoplanets. Exoplanet detection by direct imaging is a challenging task for three main reasons: (1) the host star is several orders of magnitude brighter than exoplanets, (2) the angular distance between exoplanets and star is usually very small, and (3) the images are affected by the noises called speckles that are very similar to the exoplanet signal both in shape and intensity. We first empirically examine the statistical noise assumptions of the L1 and L2 models, and then we evaluate the performance of the proposed L1 low-rank approximation (L1-LRA) algorithm based on visual comparisons and receiver operating characteristic (ROC) curves. We compare the results of the L1-LRA with the widely used truncated singular value decomposition (SVD) based on the L2 norm in two different annuli, one close to the star and one far away.

**Keywords:** L1 norm · low-rank approximation · Laplace distribution · direct imaging · exoplanet detection

## 1 Introduction

In the field of exoplanet detection, the vast majority of planets (about 99%) have been detected by indirect methods. Over the past decade, we have observed the rapid development of high-contrast imaging as a promising technique for the detection of exoplanets. Although very challenging, direct imaging provides two main advantages compared to indirect methods. First, it gives access to the photons of the planets, so we can obtain information about the atmospheric

---

<sup>\*</sup> This work was supported by the Fonds de la Recherche Scientifique-FNRS under Grant no T.0001.23. Simon Vary is a beneficiary of the FSR Incoming Post-doctoral Fellowship.

composition of the planets [2]. Second, direct imaging allows us to capture images of planets in a matter of hours, while indirect methods can take years, as they often depend on observing the orbital motion of planet around its host star. This temporal efficiency becomes especially critical when searching for planets with wider orbits. Indirect methods may require an extended duration to detect planets in these regions, while direct imaging opens up opportunities for their discovery.

Due to the small angular separation between the host star and potential exoplanets, direct imaging requires high-resolution images and, therefore, large and high resolution ground-based telescopes. This causes the light to be diffracted by atmospheric turbulence as it passes through the atmosphere. Despite the use of coronagraphs, such as the well-known Lyot coronagraph or, more recently, vortex coronagraphs [16], to reduce the high contrast caused by the brightness of the star and adaptive optics techniques to avoid the aberrations caused by the refraction of the light, standard signal processing methods may still be unable to detect the planet in the images, due to the residual aberrations in the form of quasi-static speckles that are often brighter than the planet and resemble the planet in shape.

Angular differential imaging (ADI) is a widely used technique in astronomy to reduce the effects of speckle noise in the images [14]. This technique is based on observations made in pupil tracking mode, in which the star is fixed in the center of the images as the Earth rotates in a night, which causes the exoplanet to rotate around the host with time. ADI aims at building a reference point spread function (PSF) that reproduces a model of the speckle field to be subtracted from the images and aligned (in some methods, also combined) with the signal of potential exoplanets.

Several algorithms are used to build the reference PSF in ADI. The most popular ones are based on low-rank approximations to build the reference PSF: principal component analysis (PCA) [19,1], its annular version (AnnPCA) [12,4], non-negative matrix factorization [18], the local low-rank plus sparse plus Gaussian decomposition (LLSG) [11], and more recently low-rank plus sparse trajectory [20]. Regime-switching model [7] also combines the advantages of numerous PSF subtraction techniques using low-rank approximations.

Methods based on the low-rank assumption are obtained by transforming the data cube into a matrix such that each frame corresponds to a row of the matrix. In the cases where we fit the low-rank approximation by minimizing the Frobenius norm, i.e., by PCA (or equivalently, truncated SVD), this corresponds to the maximum likelihood estimator under the i.i.d. white Gaussian noise assumption. However, several recent lines of work observed that the residual datacube, which is obtained by subtracting the low-rank part from the original data, is more compatible with the Laplacian distribution that has heavier tails instead of Gaussian [17,6].

In this paper, we propose to perform the low-rank background approximation using the component-wise L1 norm and to apply a data-dependent approximation. This approach leverages two distinct annuli in the frames, one close and

the other far from the star. Firstly, it involves an analysis of the data to identify whether the data is better fitted by a Gaussian or Laplacian distribution. Subsequently, we compare the results both visually and through ROC curve analysis.

The rest of this paper is structured as follows. In Section 2, we propose an alternative to PCA in the context of exoplanet detection, namely a component-wise L1 norm low-rank matrix approximation. We investigate different statistical assumptions on the data and analyze the performances, then apply the appropriate low-rank approximation to the data and present the experimental results in Section 3. Finally, we conclude in Section 4 and discuss potential future works.

## 2 Models and Methods

### 2.1 Planet flux estimation

Let  $M \in \mathbb{R}^{T \times N^2}$  be a matrix of observations that consists of  $T$  unfolded frames with size  $N \times N$ , i.e., each row of the matrix represents a single vectorized frame. The model for  $M$  proposed in [6], assuming a single planet located at position  $g \in [N] \times [N]$  in the first frame, is expressed as

$$M = L + a_g P_g + E, \quad \text{rank}(L) \leq k, \quad (1)$$

where  $L$  is the low-rank background,  $E$  is the noise,  $a_g$  is the intensity of the planet referred to as the *flux*,  $P_g$  is the planet signature along the trajectory.

For such models based on low-rank approximations, the choice for the rank value is crucial. Indeed, if the rank is too small, the signal of the speckles will remain in the residual  $M - L$ , making it difficult to separate the signal of the planet from the speckles. Conversely, if it is too large, the signal of the planet will be captured by the low-rank matrix, and it will be challenging to find the signal of the planets in the residual.

When the error  $E$  is Gaussian distributed, the maximum likelihood estimator for  $L$  is obtained by the minimization of the Frobenius norm. Classical methods, such as AnnPCA and LLSG, fit the low-rank component as follows:

$$\hat{L} = \arg \min_L \|M - L\|_F \quad \text{subject to} \quad \text{rank}(L) \leq k, \quad (2)$$

where  $\|A\|_F$  denotes the entry-wise L2-norm of  $A$  (the Frobenius norm), which can be solved using the truncated SVD. This step is followed by subtracting the low-rank component and identifying the planet  $a_g P_g$  in the residual matrix by solving the minimization problem

$$\hat{a}_g = \arg \min_{a_g > 0} \|M - \hat{L} - a_g P_g\|_2, \quad (3)$$

for all possible  $P_g \in \mathcal{A}$ .

In order to detect the presence of a planet, (3) has to be solved for all planet positions  $g$  of potential interest, which are all the pixels except for the ones that are too close to the star and those located at the corners since they cannot adequately capture the rotational motion of the planet; see Section 2.2 for the detection step.

Recently, it has been observed that the error term  $E$  has heavy tails and more closely follows the Laplacian distribution [17]. Consequently, it was proposed in [6] to identify the planet using L1 minimization

$$\hat{a}_g = \arg \min_{a_g > 0} \|M - \hat{L} - a_g P_g\|_1, \quad (4)$$

where  $\|\cdot\|_1$  is the component-wise L1 norm, that is,  $\|M\|_1 = \sum_{i,j} |M[i,j]|$ .

However, this approach introduces an inconsistency in the noise assumption between the speckle subtraction (2) and planet identification (4). While L1 minimization proves effective for planet identification, it raises the question of why not apply the L1 norm to background subtraction as well.

Consequently, we propose to fit the low-rank component using the component-wise L1 norm

$$\hat{L} = \arg \min_L \|M - L\|_1 \quad \text{s.t.} \quad \text{rank}(L) \leq k, \quad (5)$$

followed by the planet estimation in L1 norm as stated in (4). This approach allows us to maintain a consistent noise assumption across both the low-rank speckle subtraction and the planet estimation phases. By doing so, we aim to enhance the overall integrity and reliability of the analysis.

In fact, the proposed approach consists of addressing the optimization problem

$$\min_{L, a_g} \|M - L - a_g P_g\|_1 \quad \text{subject to} \quad \text{rank}(L) \leq k$$

by first minimizing over  $L$ , then minimizing over  $a_g$ . (An interesting direction for future work would be to consider alternating minimization. Preliminary results can be found in [5].)

The L1 low-rank approximation in (5) is an NP-hard problem, even in the rank-one case [10]. Hence, most algorithms to tackle (5), such as alternating convex optimization [13], the Wiberg algorithm [8], and augmented Lagrangian approaches [21], do not guarantee to find a global optimal solution, unlike in the case of PCA. Moreover, the computed solutions are sensitive to the initialization of the algorithms.

We use Algorithm 1 (L1-LRA) suggested by [10] to solve (5). It solves the problem using an exact block cyclic coordinate descent method, where the blocks of variables are the columns of  $\hat{U}$  and the rows of  $\hat{V}$  of the low-rank approximation  $\hat{L} = \hat{U}\hat{V}$ . We initialized the algorithm with the truncated SVD solution, denoted by  $H_k^{\text{SVD}}(\cdot)$  in Algorithm 1. In our experiments, we apply an annular version, similar to annular PCA (AnnPCA) [12,4], that selects only the pixels of



$M$  in a certain annulus. Indeed, as the values of pixels decrease away from the star, it is usually better to calculate the low-rank approximation of each annulus separately.

---

**Algorithm 1: L1-LRA [10]**


---

**Input:** Image sequence  $M \in \mathbb{R}^{t \times n}$ , rank  $k$ , maximum number of iteration  
maxiter  
1  $\hat{U}, \hat{S}, \hat{V}^T = H_k^{\text{SVD}}(M)$   
2  $\hat{U} = \hat{U}\hat{S}; \quad \hat{V} = \hat{V}^T$   
3 **for**  $i = 1$ : maxiter **do**  
4      $R = M - \hat{U}\hat{V}$   
5     **for**  $j = 1 : k$  **do**  
6          $R = R + \hat{U}[:, j]\hat{V}[j, :]$   
7          $\hat{U}[:, j] = \min_u \|R - u\hat{V}[j, :]\|_1$   
8          $\hat{V}[j, :] = \min_v \|R^T - v\hat{U}[:, j]\|_1^T$   
9          $R = R - \hat{U}[:, j]\hat{V}[j, :]$   
10     **end**  
11 **end**

---

To solve the minimization problem in steps 7-8 of Algorithm 1, we use the exact method from [9]; these subproblems are weighted median problems which can be solved in closed form.

## 2.2 Planet detection

The detection procedure consists of declaring positive the positions  $g$  where a detection metric—e.g., an SNR or a likelihood ratio—exceeds a given threshold. A likelihood ratio map  $\Lambda$  was proposed in [6], which consists of L1 norm likelihood ratios  $\Lambda_g(R)$  based on maximizing log-likelihood of Laplace distribution using the solution of (3) or (4) because it has been shown to provide better results in practice [6]

$$\log \Lambda_g(R) = - \sum_{(t,r) \in \Omega_g} \frac{|R(t,r) - \hat{a}_g P_g(t,r)| - |R(t,r)|}{\sigma_{R(r)}}, \quad (6)$$

where  $R = M - \hat{L}$ ,  $\sigma_R$  is the standard deviation of  $R$  computed along the time dimension, and  $\Omega_g$  is the set of indices  $(t,r)$  of pixels whose distance from the trajectory is smaller than half the diffraction limit, for more details see [6]. We will also use the L2 norm  $\Lambda$  map which consists of L2 norm likelihood ratios

$A_g(R)$  using the solution of (3) or (4)

$$\log A_g(R) = -\frac{1}{2} \sum_{(t,r) \in \Omega_g} \frac{|R(t,r) - \hat{a}_g P_g(t,r)|^2 - |R(t,r)|^2}{\sigma_{R(r)}^2}. \quad (7)$$

### 3 Numerical Experiments

In order to analyze the performance of the L1-LRA algorithm for background subtraction in exoplanet detection, we compare the algorithms visually by plotting their log-likelihood detection maps  $\Lambda$  and also using receiver operating characteristic (ROC) curves. Additionally, we empirically investigate the methods in terms of fitting the data to Gaussian and Laplacian distributions. The Python codes of the implementations are publicly available from [https://github.com/hazandaglayan/l1lra\\_for\\_exoplanets](https://github.com/hazandaglayan/l1lra_for_exoplanets).

We tested the algorithms using the publicly available dataset *sph3* for the exoplanet data challenge [3]. The ADI cube obtained with the VLT/SPHERE-IRDIS instrument has 228 frames with size  $160 \times 160$ , and it has a total field rotation of 80.5 degrees. It is a real dataset, but it has 5 synthetically injected planets at different distances from the star.

#### 3.1 Empirical estimation of the noise distributions

In order to analyze the suitability of different noise assumptions, we fit the Gaussian and the Laplacian distribution to the residual data, i.e., the data after subtracting the low-rank component using PCA or L1-LRA. We look at two different annuli separately, one that is close to the star at  $4\lambda/D$  separation and one more distant from the star at  $10\lambda/D$  and measure the goodness of fit visually and by the coefficient of determination  $\rho^2$ .

In Figure 1, we observe that the residual data follows a Gaussian distribution after applying PCA and a Laplace distribution after applying L1-LRA in general. However, the Laplacian distribution provides a better fit for the residual cube distribution in the tails, regardless of whether PCA or L1-LRA is used, for both small and large separations.

To assess the quality of fit of a distribution to the residual data, we use the correlation of determination as a metric. The correlation of determination  $\rho^2$  quantifies the relationship between two sample sets, denoted as  $X = (x_1, \dots, x_n)$  and  $Y = (y_1, \dots, y_n)$ , and is computed as follows:

$$\rho^2 = \frac{(\sum_{i=1}^n (x_i - \bar{x})(y_i - \bar{y}))^2}{(\sum_{i=1}^n (x_i - \bar{x})^2)(\sum_{i=1}^n (y_i - \bar{y})^2)}. \quad (8)$$

where  $\bar{x}$  and  $\bar{y}$  represent the means of the variables in samples  $X$  and  $Y$ . This metric aids in comparing the goodness of fit of different distributions. A  $\rho^2$  value close to 1 indicates that the data is more consistent with the distribution. In our experiments,  $X$  represents the height of the bins of the data histogram, while  $Y$  corresponds to the values of the probability density function within these bins.

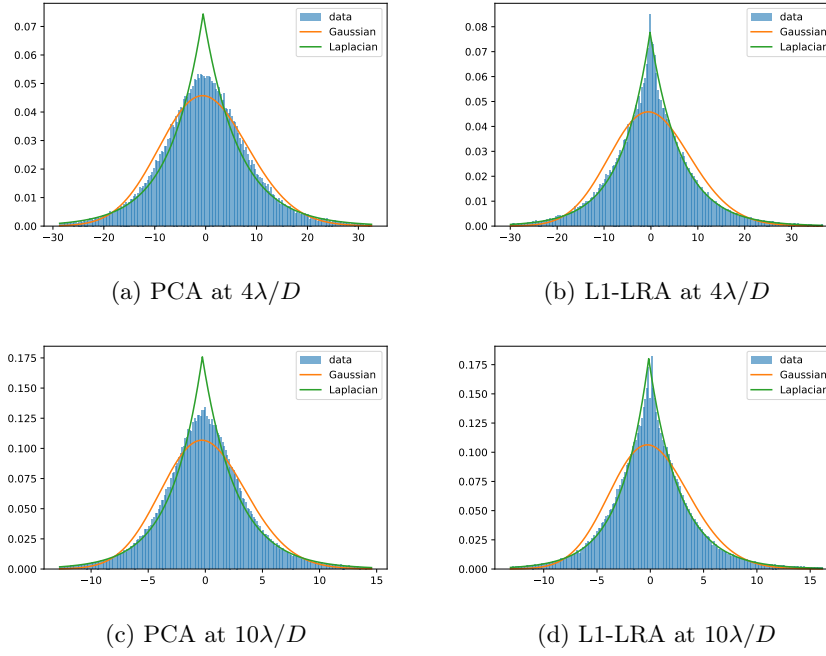


Fig. 1: Residual cube after low-rank approximation applied for small and large separations

In Table 1 and 2, we compute  $\rho^2$  value between the tails of the data distribution and the Gaussian or Laplacian distributions. The highest  $\rho^2$  is obtained with L1-LRA for both small and large separations.

Table 1: The coefficient of determination  $\rho^2$  for small separation  $4\lambda/D$

Rank	PCA		L1-LRA	
	Gaussian	Laplacian	Gaussian	Laplacian
5	0.9876	0.9918	0.9878	<b>0.9920</b>
10	0.9866	0.9890	0.9878	<b>0.9938</b>
15	0.9841	0.9948	0.9916	<b>0.9972</b>

### 3.2 Performance comparison of L1-LRA and PCA

We test the performance advantage of using the L1-LRA instead of PCA approximation in terms of visual quality and ROC curves tested on the sph3 test

Table 2: The coefficient of determination  $\rho^2$  for large separation  $10\lambda/D$ 

Rank	PCA		L1-LRA	
	Gaussian	Laplacian	Gaussian	Laplacian
5	0.9866	0.9920	0.9894	<b>0.9940</b>
10	0.9859	0.9936	0.9872	<b>0.9948</b>
15	0.9912	0.9954	0.9922	<b>0.9960</b>

data [3]. We also provide ablation studies using combinations of mixed models, where the low-rank  $L$  is first subtracted from the original data  $M$  using L1-LRA or PCA, then used in the planet detection. As such, we have four possible algorithms to investigate; see Table 3.

Table 3: Descriptions of algorithms

Background subtraction	Planet detection	
	L1 (4) and (6)	L2 (3) and (7)
L1-LRA (5)	L1L1	L1L2
PCA (2)	L2L1	L2L2

We first compared the algorithms, visually in the likelihood ratio map  $\Lambda$  map using the dataset with five synthetic planets. We selected the best performing rank according to the average likelihood ratio over the locations of the injected planets. Based on this, we chose ranks 5, 6, 5, and 10 for L1L1, L1L2, L2L1, and L2L2, respectively.

Figure 2 shows the  $\Lambda$  map and the intensity of pixels in the  $\Lambda$  map obtained with the four algorithms. In each right-hand plot, the black line shows the lowest threshold for which there is no false positive. At this threshold, we observe that L1L1 and L2L1 detect the five injected planets, whereas L1L2 and L2L2 miss one of them. Moreover, the likelihood ratios of the planet pixels (the red dots in the figures) obtained by L1L1 are much larger than the threshold.

To evaluate the performance of the four methods, we put them to the test using synthetically generated data and examine their results using ROC curves in Fig. 3. The detection map used as input for the ROC curve procedure of [6] is the  $\Lambda$  map. We deleted the five injected planets from the dataset using VIP-HCI package [12,4]. Then, we created 50 different datasets by injecting two planets in each, 180 degrees apart, and placed at the separation  $4\lambda/D$ . We set the intensity of each injected planet as  $1\sigma$  where  $\sigma$  is the standard deviation of the annulus. We applied the same procedure to a larger separation of  $10\lambda/D$  with the intensity  $0.6\sigma$ . The four methods were tested for three different rank values  $k = \{5, 10, 15\}$ .

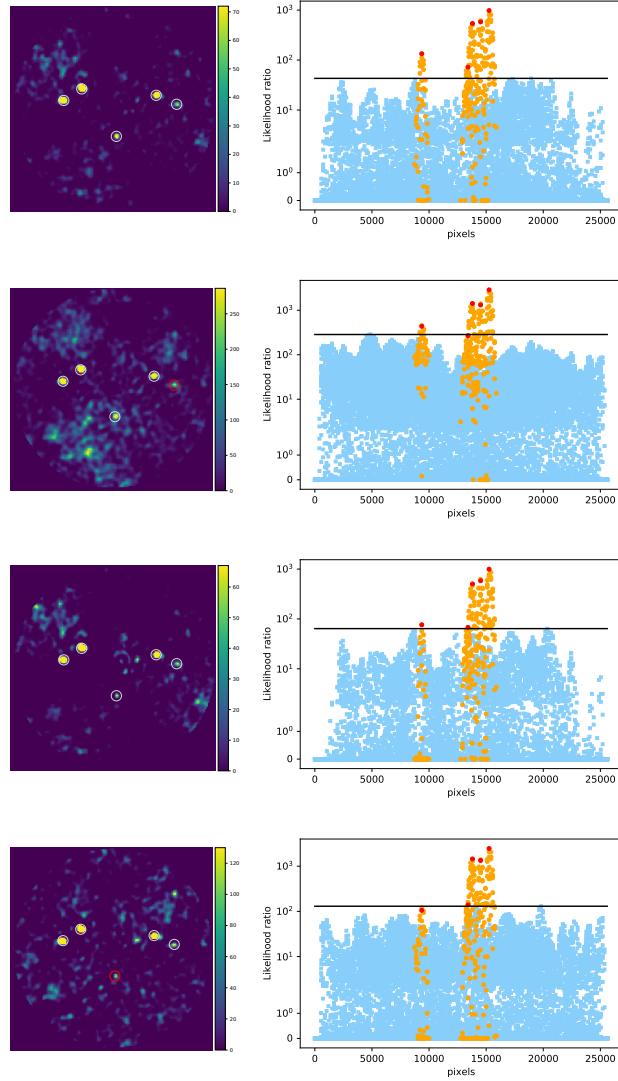


Fig. 2: Left column:  $\Lambda$  map results of the methods L1L1, L1L2, L2L1, and L2L2 from top to bottom. The detected planets are circled in white and the non-detected planets are circled in red. Right column: Intensity of the pixels in the  $\Lambda$  maps. Those maps have been flattened such that the horizontal axis corresponds to the pixels of the  $\Lambda$  map, and the vertical axis indicates the intensity of the pixels in the  $\Lambda$  map. The center pixels of the planets and the pixels near the planet are shown in thick red and orange dots, respectively. Other pixels are displayed as blue squares. The black line corresponds to the highest blue square.

In the ROC curve results, we focus on the number of true positives before the first false positives are found, as done in [6]. In the ROC curves obtained by injecting the planets at the small separation (left-hand column of Figure 3), L1L1 always gives the best results. This is also the case for the large separation with  $k = 5$  (top right plot of Figure 3). In the remaining two plots (i.e., large separation and  $k = \{10, 15\}$ ), the four algorithms perform rather similarly. Moreover, we can see a relationship between the ROC curve performances of the algorithms and the  $\rho^2$  values. L1L1, which corresponds to blue curves, has the highest  $\rho^2$  value, while L2L2, which corresponds to red curves, has the lowest value. In addition, L2L1 generally has the second-highest  $\rho^2$  value while generally performing the second-best on ROC curves.

We also compared the L1-LRA and PCA algorithms using SNR map as a detection map, which is a classical approach in direct imaging [15]. We use the implementation of SNR available in the VIP package [12,4]. Figure 4 shows the ROC curves of SNR maps applied after PCA and L1-LRA. We use the same inputs and procedure as described above. Except for the results of  $k = 5$ , L1-LRA outperforms PCA in all ROC curves for both separations.

## 4 Conclusion

In this study, we proposed a low-rank approximation algorithm in the sense of the component-wise L1-norm, termed L1-LRA, for background subtraction to detect exoplanets. A comparison with the commonly used PCA based on the L2 norm was conducted within two distinct annuli: one near the host star and the other farther away. Through empirical analysis, we examined the statistical noise assumptions of our models and evaluated the performance of the L1-LRA algorithm using visual comparisons and ROC curves. In addition to the success observed in these comparisons, our evaluation of performance metrics, including the coefficient of determination  $\rho^2$ , indicates that the L1L1 approach consistently outperforms alternatives. The proposed L1-LRA algorithm presents a promising solution for the challenging task of exoplanet detection.

There are several directions for future studies, such as using different initializations for the L1 norm approximation or designing more efficient algorithms (e.g., based on smoothing techniques). In concurrent work [5], we have investigated a technique that consists in estimating both  $L$  and  $a_g$  simultaneously in (1).

## References

1. Amara, A., Quanz, S.P.: PYNPOINT : An image processing package for finding exoplanets: PYNPOINT. *Monthly Notices of the Royal Astronomical Society* **427**(2), 948–955 (Dec 2012). <https://doi.org/10.1111/j.1365-2966.2012.21918.x>
2. Bowler, B.P., Nielsen, E.L.: Occurrence rates from direct imaging surveys. In: *Handbook of Exoplanets*, pp. 1967–1983. Springer International Publishing (2018). [https://doi.org/10.1007/978-3-319-55333-7\\_155](https://doi.org/10.1007/978-3-319-55333-7_155)

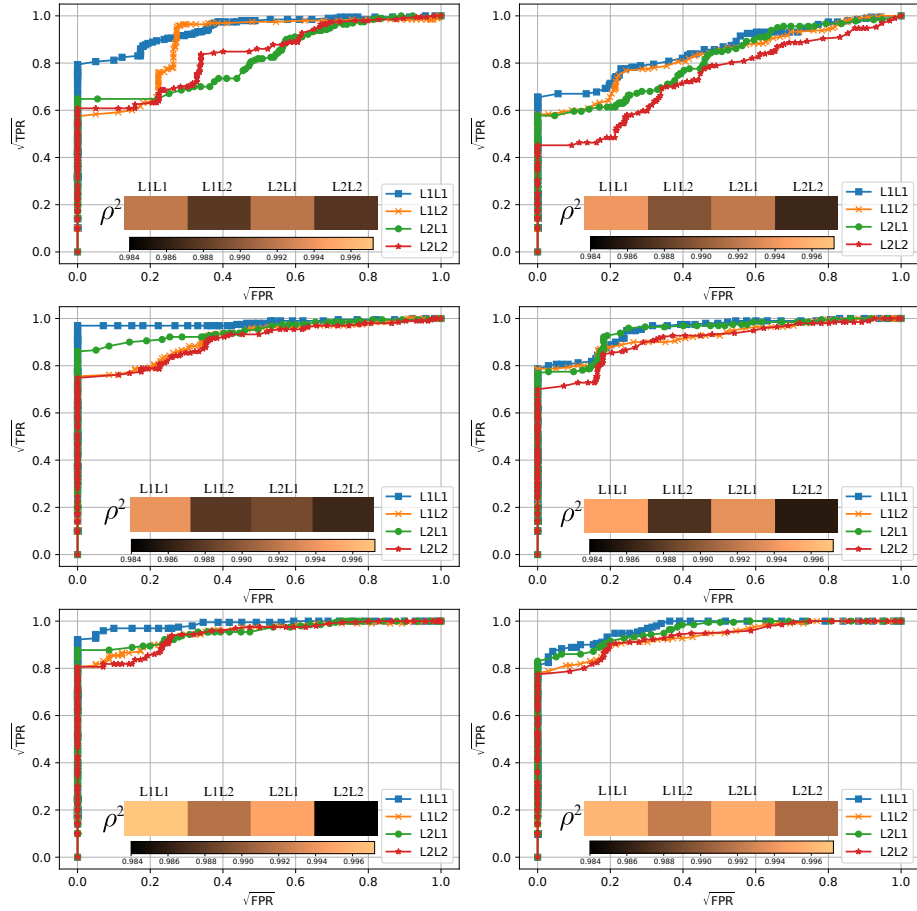


Fig. 3: ROC curves. Left column plots belong to data cubes where the planets are injected in small separation ( $4\lambda/D$ ). Right column plots belong to data cubes where the planets are injected in large separation ( $10\lambda/D$ ). The rank is 5, 10, and 15 from top to bottom. Brown bars show the coefficient of determination  $\rho^2$  for each algorithm.

3. Cantalloube, F., et al.: Exoplanet imaging data challenge: benchmarking the various image processing methods for exoplanet detection. In: Adaptive Optics Systems VII. vol. 11448, pp. 1027–1062. SPIE (2020)
4. Christiaens, V., Gonzalez, C., Farkas, R., Dahlgvist, C.H., Nasedkin, E., et al.: VIP: A Python package for high-contrast imaging. The Journal of Open Source Software **8**(81), 4774 (Jan 2023). <https://doi.org/10.21105/joss.04774>
5. Daglayan, H., Vary, S., Absil, P.A.: An alternating minimization algorithm with trajectory for direct exoplanet detection. In: ESANN 2023 proceedings, European Symposium on Artificial Neural Networks, Computational Intelligence and Machine Learning (2023). <https://doi.org/10.14428/esann/2023.ES2023-137>

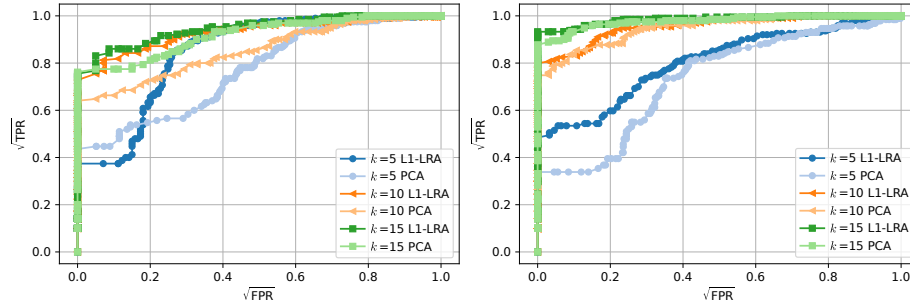


Fig. 4: ROC curves of SNR maps. The left column plot belongs to data cubes where the planets are injected in small separation ( $4\lambda/D$ ), while the right column plot belongs to data cubes where the planets are injected in large separation ( $10\lambda/D$ ).

6. Daglayan, H., Vary, S., Cantalloube, F., Absil, P.A., Absil, O.: Likelihood ratio map for direct exoplanet detection. In: 2022 IEEE 5th International Conference on Image Processing Applications and Systems (IPAS). vol. Five, pp. 1–5 (2022). <https://doi.org/10.1109/IPAS55744.2022.10052997>
7. Dahlqvist, C.H., Cantalloube, F., Absil, O.: Regime-switching model detection map for direct exoplanet detection in adi sequences. *Astronomy & Astrophysics* **633**, A95 (2020)
8. Eriksson, A., Van Den Hengel, A.: Efficient computation of robust low-rank matrix approximations in the presence of missing data using the  $\ell_1$  norm. In: 2010 IEEE Computer Society Conference on Computer Vision and Pattern Recognition. pp. 771–778. IEEE (2010)
9. Gillis, N., Plemmons, R.J.: Dimensionality reduction, classification, and spectral mixture analysis using non-negative underapproximation. *Optical Engineering* **50**(2), 027001–027001 (2011)
10. Gillis, N., Vavasis, S.A.: On the complexity of robust PCA and  $\ell_1$ -norm low-rank matrix approximation. *Mathematics of Operations Research* **43**(4), 1072–1084 (2018)
11. Gomez Gonzalez, C.A., et al.: Low-rank plus sparse decomposition for exoplanet detection in direct-imaging ADI sequences: The LLSG algorithm. *Astronomy & Astrophysics* **589**, A54 (May 2016). <https://doi.org/10.1051/0004-6361/201527387>
12. Gomez Gonzalez, C.A., et al.: VIP : Vortex Image Processing Package for High-contrast Direct Imaging. *The Astronomical Journal* **154**(1), 7 (Jun 2017). <https://doi.org/10.3847/1538-3881/aa73d7>
13. Ke, Q., Kanade, T.: Robust  $\ell_1$  norm factorization in the presence of outliers and missing data by alternative convex programming. In: 2005 IEEE Computer Society Conference on Computer Vision and Pattern Recognition (CVPR'05). vol. 1, pp. 739–746 vol. 1 (2005). <https://doi.org/10.1109/CVPR.2005.309>
14. Marois, C., Lafreniere, D., Doyon, R., Macintosh, B., Nadeau, D.: Angular Differential Imaging: A Powerful High-Contrast Imaging Technique. *The Astrophysical Journal* **641**(1), 556–564 (Apr 2006). <https://doi.org/10.1086/500401>
15. Mawet, D., Milli, J., Wahhaj, Z., Pelat, D., Absil, O., Delacroix, C., Boccaletti, A., Kasper, M., Kenworthy, M., Marois, C., Mennesson, B., Pueyo, L.: Fundamental



- limitations of high contrast imaging set by small sample statistics. *The Astrophysical Journal* **792**(2), 97 (aug 2014). <https://doi.org/10.1088/0004-637x/792/2/97>
16. Mawet, D., Riaud, P., Absil, O., Surdej, J.: Annular groove phase mask coronagraph. *The Astrophysical Journal* **632**(2), 1191 (2005)
  17. Pairet, B., Cantalloube, F., Gomez Gonzalez, C.A., Absil, O., Jacques, L.: STIM map: Detection map for exoplanets imaging beyond asymptotic Gaussian residual speckle noise. *Monthly Notices of the Royal Astronomical Society* **487**(2), 2262–2277 (Aug 2019). <https://doi.org/10.1093/mnras/stz1350>
  18. Ren, B., Pueyo, L., Zhu, G.B., Debes, J., Duchêne, G.: Non-negative matrix factorization: robust extraction of extended structures. *The Astrophysical Journal* **852**(2), 104 (2018)
  19. Soummer, R., Pueyo, L., Larkin, J.: Detection and characterization of exoplanets and disks using projections on Karhunen-Loève eigenimages. *The Astrophysical Journal* **755**(2), L28 (Aug 2012). <https://doi.org/10.1088/2041-8205/755/2/L28>
  20. Vary, S., Daglayan, H., Jacques, L., Absil, P.A.: Low-rank plus sparse trajectory decomposition for direct exoplanet imaging. In: ICASSP 2023-2023 IEEE International Conference on Acoustics, Speech and Signal Processing (ICASSP). pp. 1–5. IEEE (2023)
  21. Zheng, Y., Liu, G., Sugimoto, S., Yan, S., Okutomi, M.: Practical low-rank matrix approximation under robust l1-norm. In: 2012 IEEE Conference on Computer Vision and Pattern Recognition. pp. 1410–1417. IEEE (2012)